

Use of Deep Learning for Characterization of Microfluidic Soft Sensors

Seunghyun Han¹, Taekyoung Kim², Dooyoung Kim¹, Yong-Lae Park², and Sungho Jo¹

Abstract—Soft sensors made of highly deformable materials are one of the enabling technologies to various soft robotic systems, such as soft mobile robots, soft wearable robots, and soft grippers. However, major drawbacks of soft sensors compared with traditional sensors are their nonlinearity and hysteresis in response, which are common especially in microfluidic soft sensors. In this research, we propose to address the above issues of soft sensors by taking advantage of deep learning. We implemented a hierarchical recurrent sensing network, a type of recurrent neural network model, to the calibration of soft sensors for estimating the magnitude and the location of a contact pressure simultaneously. The proposed approach in this letter were not only able to model the nonlinear characteristic with hysteresis of the pressure response, but also find the location of the pressure.

Index Terms—Soft Material Robotics, Deep Learning in Robotics and Automation, Force and Tactile Sensing

I. INTRODUCTION

SOFT robotics has recently drawn keen attention and been implemented to a wide range of robotics applications that require increased interactions with surrounding environments. For example, soft grippers [1], [2] and soft mobile robots are specialized to easily adapt themselves to uncertain objects or terrains. Soft wearable robots [3], [4] and soft haptic devices [5] focus on physical interactions with the human body. In such systems, soft sensors made of highly deformable materials are one of the enabling technologies. Various types of soft sensors have been developed using hyperelastic materials embedded with electrically conductive agents, such as carbon particles [6], [7], silver nanowires [8], [9], room-temperature liquid metals [10], [11], and ionic liquids [12], [13]. All the above sensors have their own characteristics that could be useful in different situations. However, two major

Manuscript received: September 10, 2017; Revised November 27, 2017; Accepted December 26, 2017.

This paper was recommended for publication by Editor Yu Sun upon evaluation of the Associate Editor and Reviewers' comments. This work was supported in part by the National Research Foundation of Korea (NRF) Grant funded by the Korean Government (MSIT) under Grant NRF-2016R1A5A1938472 and in part by Institute for Information & communications Technology Promotion (IITP) Grant funded by the MSIT (No.2017-0-01778). (Seunghyun Han and Taekyoung Kim contributed equally to this work.) (Corresponding authors: Yong-Lae Park and Sungho Jo)

¹Seunghyun Han, Dooyoung Kim, and Sungho Jo are with School of Computing, KAIST, Daejeon 305-701, Republic of Korea. {shann, dykim07, shjo}@kaist.ac.kr

²Taekyoung Kim and Yong-Lae Park are with the Department of Mechanical and Aerospace Engineering and Institute of Advanced Machines and Design (IAMD), Seoul National University, Seoul 08826, Republic of Korea {kimtkm, ylpark}@snu.ac.kr

Digital Object Identifier (DOI): see top of this page.

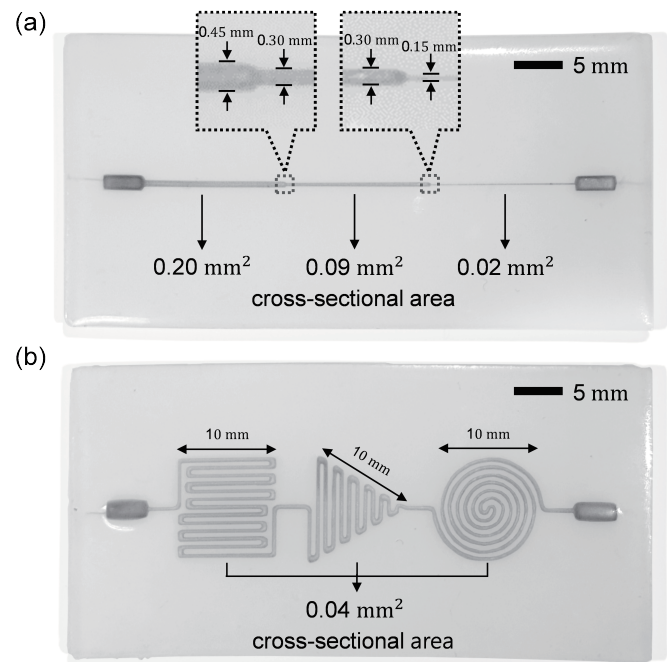


Fig. 1. The prototypes of soft pressure sensors, (a) showing the microchannel having three different cross-sectional areas, (b) showing the microchannel having three different patterns.

common drawbacks of soft sensors compared with traditional sensors are their nonlinearity and hysteresis in response, which are easily seen especially in microfluidic soft sensors [11], [14]. These characteristics sometimes limit the use of the soft sensors in spite of other advantages, since it is very difficult to characterize them not only analytically but also experimentally. Although different approaches, such as changing microchannel geometries [11] and by embedding solid particles [15], have been proposed to address these issues in design, they solved problems only partially.

Another limitation comes with arrangement of signal wires. If multiple sensors are to be placed in a limited space, there always exists a problem of connecting and routing multiple wires. Although the sensor itself is compact and soft, the signal wires to each sensing element makes the entire system complex and not completely soft.

In this research, we propose to address the above issues of soft sensors by taking advantage of deep learning. We introduced a hierarchical recurrent sensing network, a type of recurrent neural network (RNN) model, in the calibration stage for estimating the magnitude and the location of a con-

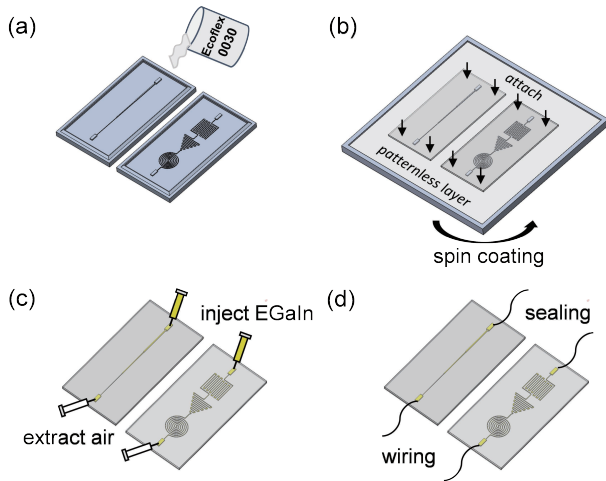


Fig. 2. Fabrication process of the soft pressure sensor (a) making patterned layers, (b) bonding process to make complete microchannel, (c) injecting liquid metal into microchannel, (d) inserting signal wires into the channels and sealing process.

tact pressure simultaneously, since RNNs have demonstrated remarkable advances for modeling temporal data over the past decade [16], [17].

In order to acquire data in our learning process, two soft pressure sensor samples were prepared, as shown in Fig. 1. The first had a single straight microchannel with three different cross-sectional areas in three segments, and the other had a single-sized microchannel but with three different patterns in different locations. The sensor samples were tested by compressing the top surface with various speeds and pressures. The location of the pressure was also varied during the test. Using our custom RNN algorithm, the proposed approach in this letter was not only able to model the nonlinear characteristic with hysteresis of the pressure response, but also find the location of the pressure.

The rest of this letter is as follows. Section II describes the preparation of soft sensor samples and the experimental setup. Section III discusses the structure of the estimation model and the learning mechanism employed in this research, and Section IV presents the analysis of the results. We discuss limitations of the current approach and future work in Section V and finally conclude our research in Section VI.

II. MATERIALS

A. Sensor Design

We designed sensor samples with various dimensions of microchannels. A total of two pressure sensors with a single microchannel filled with a liquid metal (eutectic gallium-indium or EGaIn) were fabricated. The first had a straight channel with three different cross-sectional areas (0.20 mm^2 , 0.09 mm^2 , and 0.02 mm^2) in three different segments, as shown in Fig. 1-a, and the other had a single-sized (0.04 mm^2) channel with three different serpentine patterns (square, triangle, and circle), as shown in Fig. 1-b. The microchannels of both sensors had square cross-sections and they were embedded in a $30 \text{ mm} \times 70 \text{ mm}$ rectangular elastomer matrix that had a 1 mm thickness.

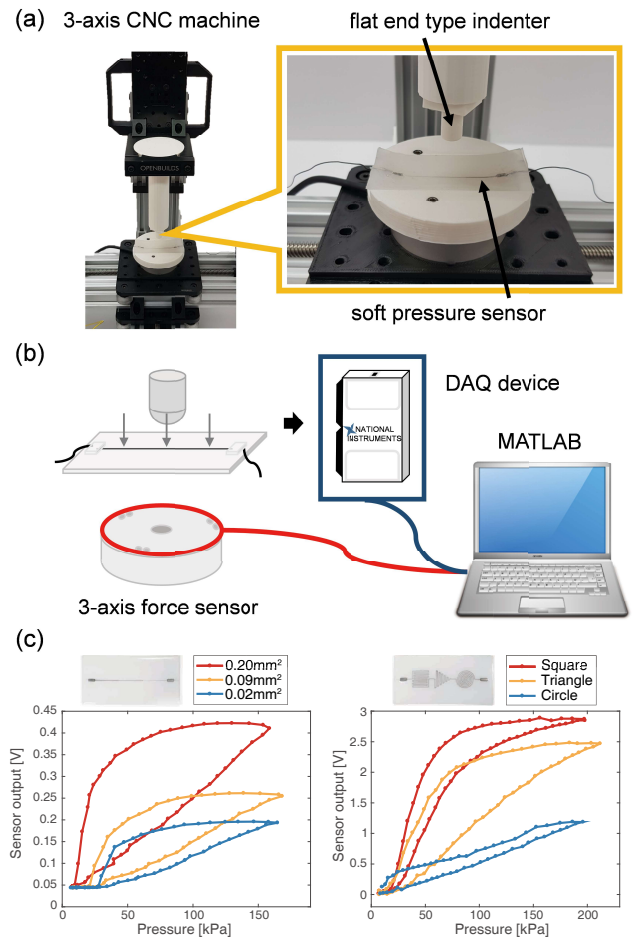


Fig. 3. Experiment setup. (a) CNC milling machine with a flat end type indenter. (b) Schematic diagram of the data acquisition. (c) Hysteresis and nonlinear characteristics of soft sensor samples with 1 mm/s of compression rate in different locations.

B. Sensor Fabrication

The sensor samples were fabricated using the layered molding and casting process developed in previous work [10]. Molds with an embossed pattern were made using a 3D printer (Object 30, Stratasys). Polymer layers with embedded microfluidic channels were made by pouring liquid silicone elastomer (Ecoflex 0030, Smooth-On) in the molds (Fig. 2-a). A patternless polymer layer was made using 3D printed patternless mold, and a thin silicone film was formed on the pattern-free layer by spin-coating. Then, the thin film was partially cured to be an adhesive agent on the patternless layer. The layers with microchannels were then attached to the sticky surface of the patternless layer (Fig. 2-b). The layers were then baked in a convection oven at 60°C until the two layers fully bond to each other. After curing, EGaIn was injected into the microchannel using hypodermic syringes (Fig. 2-c). Finally, wires were inserted into the ports of the channels, and the periphery of the wiring were sealed to prevent the liquid metal from leaking (Fig. 2-d).

TABLE I
CHARACTERISTICS OF DATASET

	Max Pressure (kPa)	Pressing Speed (mm/s)	Number of Trials
Training Data	50, 100, 190	1,2,3,4,5	46 per option in each location
Test Data	random from 50–190	random from 1–5	125 per location with random option

C. Experimental Setup

The experimental setup for acquiring training data is shown in Fig. 3. The soft sensor was mounted on a three-axis commercial load cell (RFT60-HA, Robotous). A cylindrical indenter (radius: 5 mm) attached to a motorized test stand that was modified from a tabletop CNC milling machine (MiniMill, OpenBuilds) applied vertical pressure (Fig. 3-a) to the different locations of the sensor with varied speeds. The pressure deformed and decreased the cross-section of the microchannel and consequently increased the channel’s electrical resistance [14]. The change in resistance was detected by a simple voltage divider circuit, and the data was collected using a data acquisition (DAQ) device (USB-6211, National Instrument). At the same time, the actual force applied to the soft sensor was measured by the commercial load cell. The pressure data from both the soft sensor and the commercial load cell were collected at 20 Hz. The data was transferred to the PC via serial communication using MATLAB. There was no filtering or post-processing applied to the data in this stage. Fig. 3-b shows a schematic diagram of the setup, and Fig. 3-c shows the sensor signals including hysteresis and nonlinear characteristics of the soft sensor.

D. Data Acquisition

1) *Training Data*: To obtain training data sets that reflect different pressure conditions, experiments were carried out by loading and unloading the sensor with varied pressure levels. Different pressures were applied by controlling the depth of the indenter. Three pressure levels, 50 kPa, 100 kPa, and 190 kPa, were selected in our experiments. The rate of the pressure was varied from 1 mm/s to 5 mm/s with an increment of 1 mm/s. With the above conditions, each location of the three segments in each sensor sample was pressed 46 times, making the total of 2,070 training data sets for each sensor.

2) *Test Data*: The test data were collected in the entire range of the training conditions. Random pressures between 50 kPa to 190 kPa were applied to the sensor, and the pressure rates were also randomly selected between 1 mm/s and 5 mm/s. Each location of the three different segments in each sensor was pressed 125 times, making the total of 375 test data sets for each sensor.

Summaries for the training and the test data are shown in Table I. We applied these parameters to both samples in the same way.

III. METHODS

Linear combinations are impractical for modeling the nonlinear and complex relationships between the analog voltage

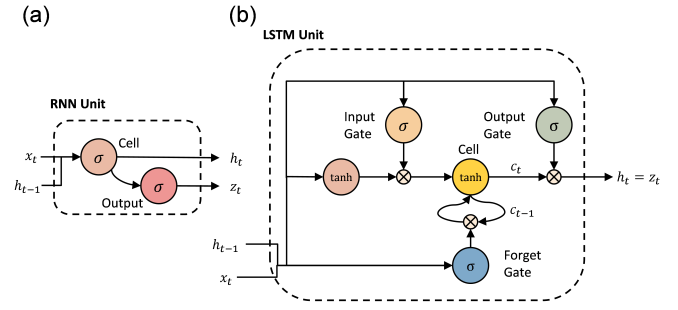


Fig. 4. (a) The structure of a RNN unit. (b) An LSTM cell (derived from the initial LSTM design proposed in [19].)

outputs and the input pressures. We predicted the magnitudes and their locations simultaneously using a single neural network that can handle temporal dynamics.

A. Recurrent Neural Network

A RNN is a type of neural network particularly well suited for modeling sequential phenomena. At each time step t , the RNN takes the n dimensional input vector $x_t \in \mathbb{R}^n$ and the previous hidden state $h_{t-1} \in \mathbb{R}^m$ which is an m dimensional vector. It learns to produce the hidden state h_t via the following recurrence equation:

$$h_t = f(Wx_t + Uh_{t-1} + b) \quad (1)$$

where f is an element-wise nonlinearity, such as a sigmoid or hyperbolic tangent, and $W \in \mathbb{R}^{m \times n}$, $U \in \mathbb{R}^{m \times m}$ and $b \in \mathbb{R}^m$ are parameters to connect each states. A RNN unit is shown in Fig.4-a. In theory, the hidden state h_t contains information about whole past sequences and it produces an output $z_t \in \mathbb{R}^m$ that reflects all histories. In practice, however, there are some limits to learning long-range dependencies due to the vanishing and exploding gradients problem [18] which is caused by the Jacobian’s multiplicativity with respect to time. This can result in an extremely nonlinear behavior of recurrent network.

As a special RNN structure, Long Short-Term Memory (LSTM) provides a stable and powerful solution by adding some controllable gates that allow the network to learn when to forget previous hidden states and when to update hidden states given new information. Fig. 4-b indicates a cell of LSTM. It produces cell vector $c_t \in \mathbb{R}^n$ given the inputs x_t , h_{t-1} and c_{t-1} by using the following operations:

$$\begin{aligned} i_t &= \sigma(W^i x_t + U^i h_{t-1} + b^i) \\ f_t &= \sigma(W^f x_t + U^f h_{t-1} + b^f) \\ o_t &= \sigma(W^o x_t + U^o h_{t-1} + b^o) \\ g_t &= \tanh(W^g x_t + U^g h_{t-1} + b^g) \\ c_t &= f_t \odot c_{t-1} + i_t \odot g_t \\ h_t &= o_t \odot \tanh(c_t) \end{aligned} \quad (2)$$

where $\sigma(\cdot)$ and $\tanh(\cdot)$ are the element-wise sigmoid and hyperbolic tangent activation functions, and \odot is an element-wise multiplication operation. The vector $i_t \in \mathbb{R}^n$, $f_t \in \mathbb{R}^n$ and $o_t \in \mathbb{R}^n$ respectively denote input gates, forget gates and output gates for controlling data flow inside the cell. W^k , U^k and

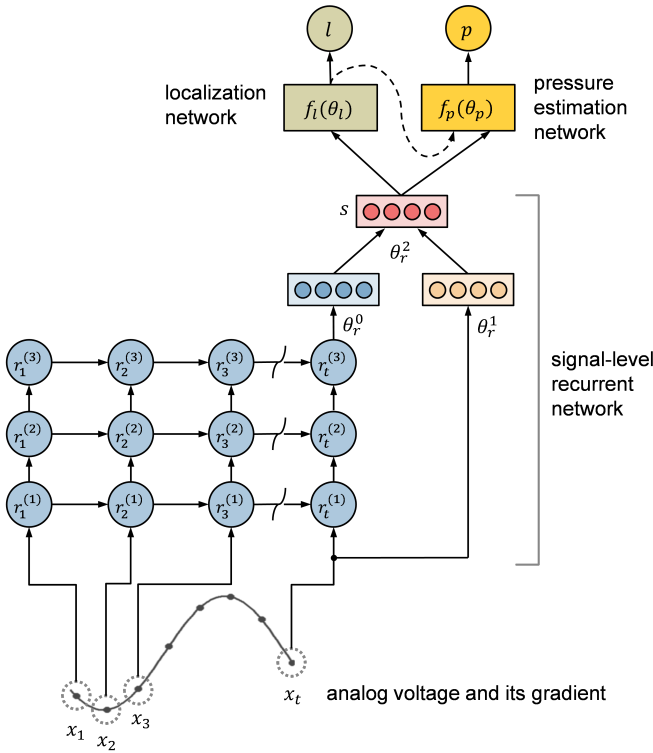


Fig. 5. The structure of the hierarchical recurrent sensing network.

b^k where $k \in \{i, f, o\}$ are parameters for each of the gates. These additional cells make the LSTM capable of learning extremely complex and long-range temporal data that a RNN simply cannot learn properly. LSTMs have been successfully proven to outperform RNNs on many tasks such as language modeling [17] and sequence generation [20].

B. Hierarchical Recurrent Sensing Network

We now present our hierarchical recurrent sensing network. Our model can concurrently learn to estimate both pressure magnitude and location while considering the hysteresis problem. It is composed of three modular networks so as to enable multi-task learning in a single structure. Fig. 5 illustrates our hierarchical recurrent sensing network architecture.

1) *Signal-level Recurrent Network*: At the beginning, the signal-level recurrent network (SigRN) transforms the sequential input data to a representation where learning of temporal dynamics is easy. It aggregates temporal information with three recurrent layers. We use LSTM units for recurrent layers and denote each layer as $r^{(1)}$, $r^{(2)}$ and $r^{(3)}$. At each time step t , vector x_t which includes raw voltage and gradient of signal, of a sequence $X = (x_1, \dots, x_t)$ passes through the three LSTM layers to produce temporal representation. The temporal representation and the last input x_t are then mapped into a hidden space using independent, fully connected layers parameterized by θ_r^0 and θ_r^1 , respectively, using rectified units followed by another fully connected unit θ_r^2 to combine the information from both components. It produces sensing feature s given historical input vectors and note that it can infer both temporal and actual features at the same time. We

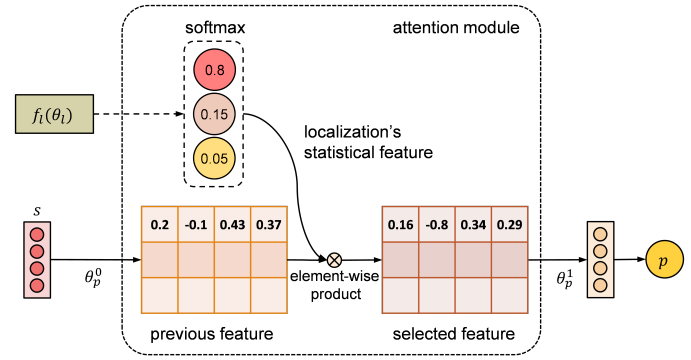


Fig. 6. The attention mechanism for the pressure estimation network.

explicitly let the following two networks consider both features to enhance performance across following estimation tasks, especially the task of pressure estimation. This empirically reduces some estimation errors around peak of sensor outputs in a pressing trial when predicting magnitude of pressures.

2) *Localization Network*: The localization network generates a predicted location l for which location on the soft pressure sensor is being pressed. The localization network $f_l(\theta_l)$ has a fully connected layer and a softmax layer. The fully connected layer takes the sensing feature s of the SigRN and produces new features which can hold suitable properties for localization. The softmax layer generates classification probabilities which corresponds to those of the pressing location. Then, the location which has the largest probability is inferred as being pressed at that time.

3) *Pressure Estimation Network*: The pressure estimation network predicts the magnitude of pressure p corresponding to sensor outputs which are analog voltages. We defined the pressure estimation network as $f_p(\theta_p)$. The feature s from the SigRN pass through an attention module and two separate, fully connected layers parameterized by θ_p^0 and θ_p^1 respectively. Fig. 6 indicates the architecture of the pressure estimation network and the attention mechanism. When the fully connected layer with parameter θ_p^0 encodes the sensing feature s into the number of localization classes, it is multiplied with class probabilities from a softmax layer from $f_l(\theta_l)$ using an element-wise product. In this way, the statistical attributes for localization can also be utilized for the pressure estimating procedure which lets the model learn what to attend to based on the locational features.

C. Learning

Our model is composed of an end-to-end optimization over a hierarchical structure. The training cost with two independent functional networks, the localization network and the pressure estimation network, are combined into a single cost function so that the model can learn to handle both tasks. In particular, the localization network uses the cross entropy objective function and the pressure estimation network uses the mean squared error (MSE) function to measure the loss between the predicted and the ground truth value for each task. These two are fused by simple addition. Also, dropout [21] is applied to each LSTM layer (except on the last LSTM layer) with a 50%

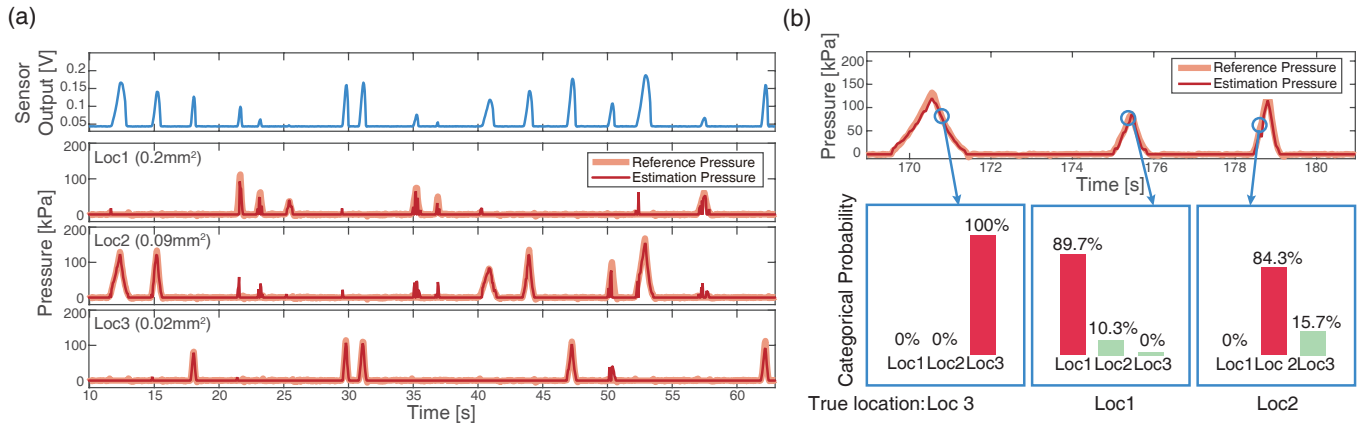


Fig. 7. (a) Results of both pressure estimation and localization using test data of three different cross-sectional channel areas. It separates the pressure estimation signals into three parts based on the localization results. (b) A selection of localization procedures and results of a categorical distribution for each case.

dropout rate to prevent the model from overfitting our training dataset.

IV. RESULT

We evaluated our model with two different datasets from the two sensor samples to assess the ability of estimating both contact pressure and location. The first sample has various cross-sectional areas on its channel, and the other has different patterns with a uniform dimension. Processing the two datasets, we used an analog voltage and a gradient of its value as a two-dimensional input. Training is performed with a stochastic gradient descent (SGD), and we trained for 100 epochs on both datasets. The model was trained using the Adam optimizer [22] with a base learning rate of 0.001. Each update was done by using 40 sequence lengths, and components of each sequences comprised voltages which have a value over a specific threshold. In addition, 32 units were used in each LSTM, and fully connected layers except for the last layer in the pressure estimation network was interleaved with rectified unit function. We implemented the entire model into the Tensorflow framework [23].

Fig. 7 illustrates both pressure estimation and localization results with time using the test data of the three different cross-sectional channels. Loc1, Loc2 and Loc3 indicates different channel cross-sectional areas of 0.20 mm², 0.09 mm² and 0.02 mm², respectively. We divided the pressure estimation signals into three parts based on the localization results. Fig. 7-a shows our model can successfully predict a magnitude of pressure and its location simultaneously on every location considering nonlinear characteristics. Examples of localization procedures are shown in Fig. 7-b. Our model generates new categorical distribution on every input and choose the pressure location at which the categorical probability is maximized. Combining those two estimations concurrently, there were some signals that fluctuated during an iteration of pressure estimation. Since our model predicts a new location on every input, it can sometimes generate different localization results at every time step even during the same iteration.

We used a root mean squared error (RMSE) and normalized RMSE (NRMSE) as an evaluation metric to measure performance of our model as follows:

$$RMSE = \sqrt{\frac{1}{N} \sum_{i=1}^N (\hat{y}_i - y_i)^2}$$

$$NRMSE = \frac{RMSE}{y_{max} - y_{min}} \times 100\%$$

where \hat{y} is predicted values and y is true values. Moreover, we measured the accuracy for localization by counting successfully classifications with each test dataset.

A. Cross-Sectional Areas

The results of the sample are shown in Tables II and III. Our model achieved an overall NRMSE of 6.64% for estimation and obtained a localization accuracy of 81.87%. The fact that the localization accuracy of the smallest cross-sectional area (i.e. Loc3) was over 94% implies that it has a more distinctive pressure hysteresis curve compared to those of the other two locations. In addition, even though localization results of the other two areas were approximately 69% below 50 kPa, they showed over 87% of accuracy above 100 kPa.

B. Patterns

We can see that the NRMSE of pressure estimation is 5.81% and the accuracy of localization is 85.42% over all of the test cases. The performance is shown in Tables IV and V. Especially, our model achieved over 93.2% of localization accuracy on every part above 100 kPa. Having different patterns denotes that it varies the number and shape of channels inside a pressure area. It provides a bigger and more diverse overall range of the sensor's analog voltage and also makes distinctive hysteresis curves. It should be noted that the range of the analog voltages on the circular area was substantially smaller than those of the other patterns. This is because the circular pattern geometrically hinders the liquid metal from quickly

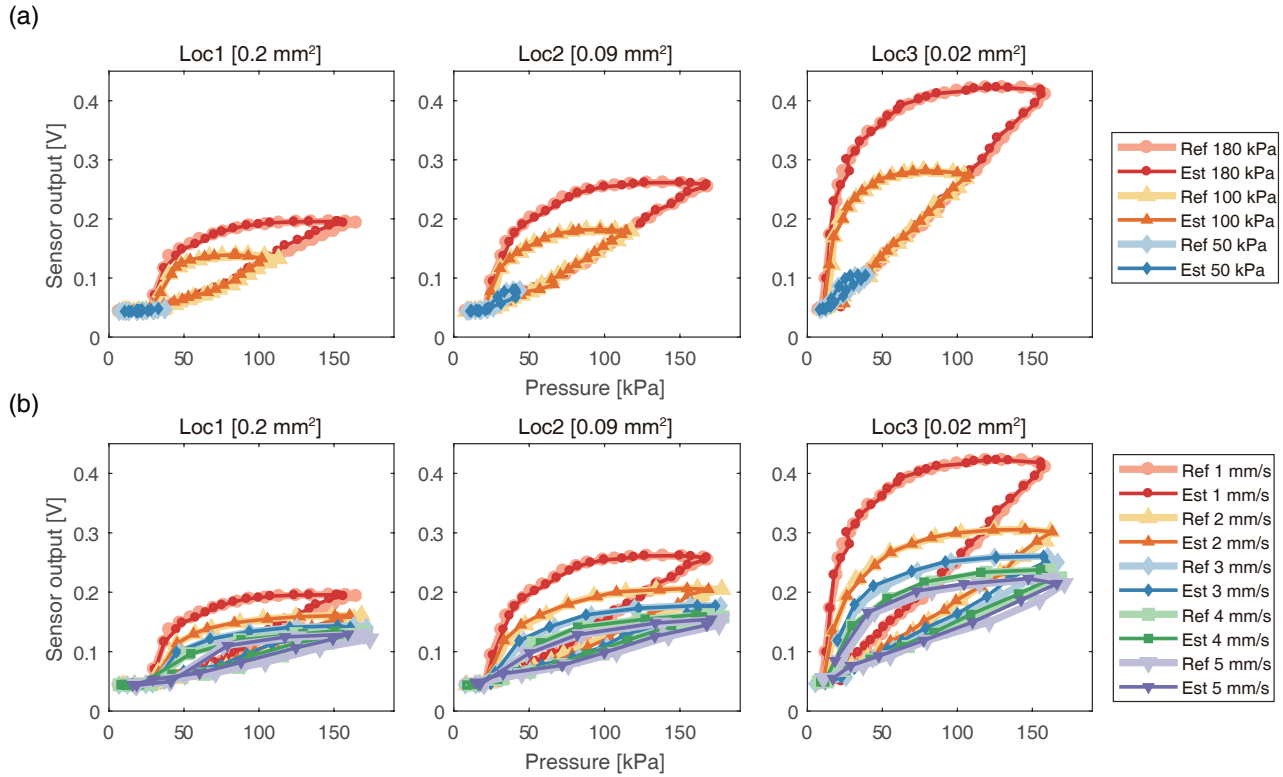


Fig. 8. Comparison between reference pressures and estimated pressures on three different cross-sectional channel areas. (a) Results from various pressures with a constant pressing speed of 1 mm/s. (b) Results from various pressing speeds with a constant pressure 180 kPa.

TABLE II
EXPERIMENTAL RESULTS OF PRESSURE ESTIMATION ON THE THREE DIFFERENT CROSS-SECTIONAL CHANNEL AREAS.

Test Error	Pressure Estimation			
	Overall	Loc1	Loc2	Loc3
RMSE (kPa)	10.81	10.43	13.59	7.91
NRMSE	6.64%	6.94%	8.38%	5%

TABLE III
EXPERIMENTAL RESULTS OF LOCALIZATION ON THE THREE DIFFERENT CROSS-SECTIONAL CHANNEL AREAS.

Test Accuracy		Predicted Location		
		Loc1	Loc2	Loc3
True Location	Loc1	75.48%	21.41%	3.11%
	Loc2	9.8%	74.59%	15.61%
	Loc3	0.58%	4.74%	94.68%
Test Accuracy	Overall	Loc1	Loc2	Loc3
0 ≤ kPa < 50	76.49%	69.15%	69.59%	90.72%
50 ≤ kPa < 100	85.28%	78.79%	77.02%	98.85%
100 ≤ kPa < 150	94.96%	97.47%	87.22%	100%
150 ≤ kPa < 180	100%	100%	100%	100%
Overall Range	81.87%	75.48%	74.59%	94.68%

moving away from the pressure area compared to the other two patterns. Due to all of the above reasons, the classification worked relatively well in all locations.

C. Further Observations

Fig. 8 and Fig. 9 show the test results of estimating pressure magnitudes and locations with varied maximum pressures and rates for the two samples, respectively. The sensor responses were highly nonlinear and hysteretic, but the estimations from our model showed good match with ground truths. During the experiments, it was observed that the lower maximum pressure makes the lower hysteresis, and the higher pressure rate yielded the lower pressure sensitivity. Therefore, our model was able to estimate the applied pressures under various conditions of pressure magnitudes and rates.

Note that the overall pressure estimation results indicate a well-fitted model on each location as shown in the Tables II and IV. Comparing with other pressure estimation results from different type of soft sensors, it is also in an acceptable range. Soft silicon pressure sensors [24] which are developed for a lower limb exoskeleton obtained a NRMSE of normal force estimation with a range of 2.7% to 8.5% and the normal and shear tactile force prediction for MIT's Cheetah's footpad sensor [25] showed a NRMSE between 1.17% and 10.14%.

In Tables III and V, localization accuracy was the highest at Loc3 and Circle for the two samples, respectively. This is because the response curves were more distinctive compared to those of the other locations in both cases, as shown in Fig.8 and Fig.9. Our model was able to catch this characteristics.

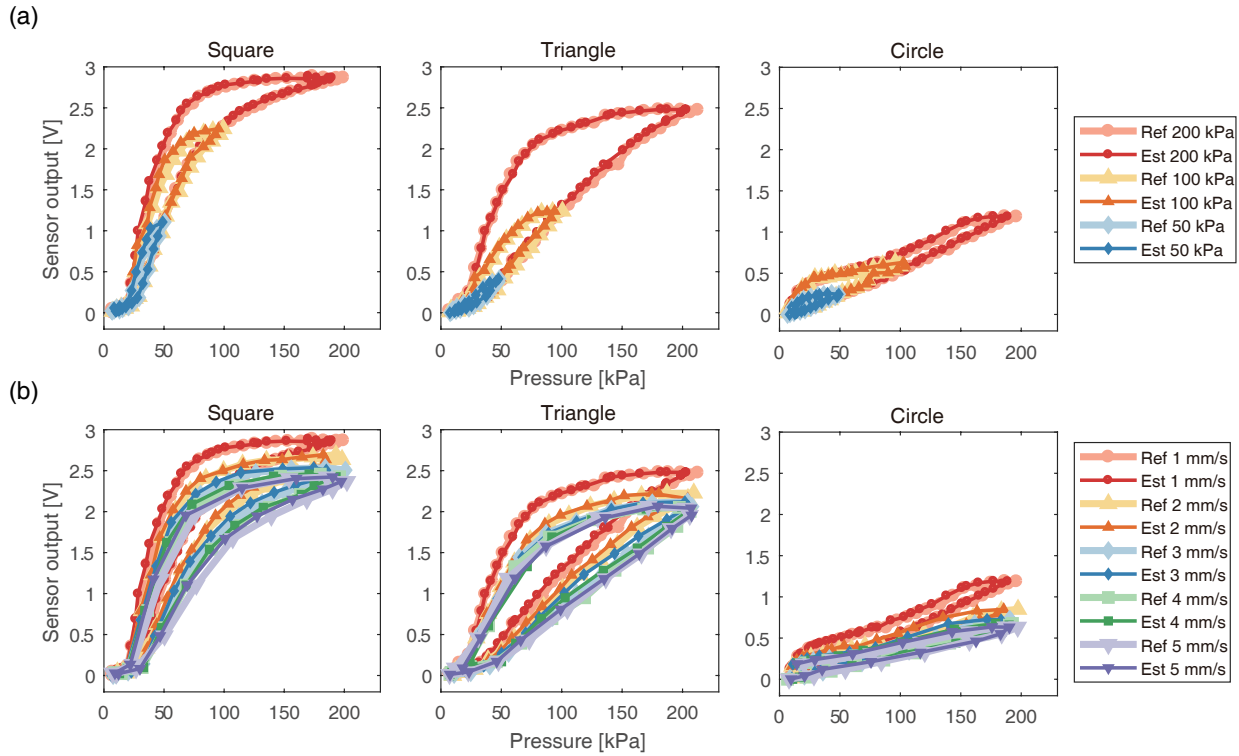


Fig. 9. Comparison between reference pressures and estimated pressures on three different patterns. (a) Results from various pressures with a constant pressing speed of 1 mm/s. (b) Results from various pressing speeds with a constant pressure 200 kPa.

TABLE IV
EXPERIMENTAL RESULTS OF PRESSURE ESTIMATION ON THE THREE DIFFERENT PATTERNS.

Test Error	Pressure Estimation			
	Overall	Square	Triangle	Circle
RMSE (kPa)	13.2	16.23	12.12	10.59
NRMSE	5.81%	7.15%	6.05%	5.12%

TABLE V
EXPERIMENTAL RESULTS OF LOCALIZATION ON THE THREE DIFFERENT PATTERNS.

Test Accuracy		Predicted Location		
		Square	Triangle	Circle
True Location	Square	84.37%	12.61%	3.02%
	Triangle	12.9%	81.47%	5.63%
	Circle	4.31%	5.28%	90.41%
Test Accuracy	Overall	Square	Triangle	Circle
0 ≤ kPa < 50	73.31%	73.42%	65.61%	80.21%
50 ≤ kPa < 100	92.58%	88.64%	90.69%	98.23%
100 ≤ kPa < 150	95.3%	94.6%	93.2%	98.38%
150 ≤ kPa < 200	97.04%	99.64%	94.02%	98.27%
Overall Range	85.42%	84.37%	81.47%	90.41%

V. DISCUSSION AND FUTURE WORK

The main contribution of this letter is tackling the modeling of problems for nonlinear signals of soft sensors using the proposed recurrent network model. Our hierarchical recurrent

sensing network showed that it could estimate the magnitude of pressure and location simultaneously for different inputs.

Although our model was able to estimate the pressure locations with relatively high accuracy, the number of locations are currently limited to the number of discrete sections in the microchannel. Therefore, one possible future improvement will be to design the microchannel to have continuous geometrical changes over its length. In this way, the localization will be also more continuous, which will expand the sensor to a two-dimensional area from the current one-dimensional line.

In addition, in this study, we performed learning using the data obtained by applying pressures to only one location of the soft sensor at a time. However, we will continue to investigate whether multiple pressures in different locations can be detected and even be localized. The result obtained from this additional study will allow us to develop a high-performance soft pressure sensor array having a small number of signal wires.

Furthermore, for our method to be more practical, the sensor should be able to estimate and localize pressures from uncontrolled indenters, such as human hands. In the current system, touch from a fingertip will generate totally different outcomes with the model that is trained by our dataset since human skin also has many nonlinear factors. Therefore, another area of future work will be to collect pressing data using a human hand with various environmental conditions that include varied temperature and humidity.

VI. CONCLUSIONS

In this letter, we proposed a method of characterizing pressure responses of microfluidic soft sensors using a deep learning scheme based on a hierarchical recurrent sensing network. The proposed method was able to not only estimate nonlinear responses with high hysteresis but also localize the contact locations. Two different sensor designs were used for testing: a straight microchannel with different cross-sectional areas in three segments and a single-sized microchannel with different patterns in three areas. In the first design, the estimation results showed an RMSE of 10.81 kPa and an NRMSE of 6.64%. The localization accuracy was 81.87%. In the second design, the results showed an RMSE of 13.2 kPa and an NRMSE of 5.81%, and the localization accuracy was 85.42%. These outcomes show that learning can simplify the calibration processes of soft sensors, and reduce the number of signal wires for a soft sensor array.

To the best of our knowledge, this is the first approach to implement RNN to estimate both contact pressure and location of soft sensors that have highly nonlinear and hysteretic characteristics. In addition, the capability of localization significantly simplifies the mechanical and electrical system by minimizing the number of signal wires in the system. Therefore, this study will create opportunities for soft sensors to be used more practically in various applications.

Our code is available at <https://github.com/seunghyunhan/deep-characterization-soft-sensor>.

REFERENCES

- [1] K. C. Galloway, K. P. Becker, B. Phillips, J. Kirby, S. Licht, D. Tchernov, R. J. Wood, and D. F. Gruber, "Soft robotic grippers for biological sampling on deep reefs," *Soft robotics*, vol. 3, no. 1, pp. 23–33, 2016.
- [2] E. Brown, N. Rodenberg, J. Amend, A. Mozeika, E. Steltz, M. R. Zakin, H. Lipsen, and H. M. Jaeger, "Universal robotic gripper based on the jamming of granular material," *Proceedings of the National Academy of Sciences*, vol. 107, no. 44, pp. 18 809–18 814, 2010.
- [3] Y.-L. Park, B.-r. Chen, N. O. Pérez-Arancibia, D. Young, L. Stirling, R. J. Wood, E. C. Goldfield, and R. Nagpal, "Design and control of a bio-inspired soft wearable robotic device for ankle-foot rehabilitation," *Bioinspiration & biomimetics*, vol. 9, no. 1, p. 016007, 2014.
- [4] Y. Mengüç, Y.-L. Park, H. Pei, D. Vogt, P. M. Aubin, E. Winchell, L. Fluke, L. Stirling, R. J. Wood, and C. J. Walsh, "Wearable soft sensing suit for human gait measurement," *The International Journal of Robotics Research*, vol. 33, no. 14, pp. 1748–1764, 2014.
- [5] S. S. Robinson, K. W. OBrien, H. Zhao, B. N. Peele, C. M. Larson, B. C. Mac Murray, I. M. Van Meerbeek, S. N. Dunham, and R. F. Shepherd, "Integrated soft sensors and elastomeric actuators for tactile machines with kinesthetic sense," *Extreme Mechanics Letters*, vol. 5, pp. 47–53, 2015.
- [6] J. T. Muth, D. M. Vogt, R. L. Truby, Y. Mengüç, D. B. Kolesky, R. J. Wood, and J. A. Lewis, "Embedded 3d printing of strain sensors within highly stretchable elastomers," *Advanced Materials*, vol. 26, no. 36, pp. 6307–6312, 2014.
- [7] M. Amjadi, Y. J. Yoon, and I. Park, "Ultra-stretchable and skin-mountable strain sensors using carbon nanotubes-ecoflex nanocomposites," *Nanotechnology*, vol. 26, no. 37, p. 375501, 2015.
- [8] M. Amjadi, A. Pichitpajongkit, S. Lee, S. Ryu, and I. Park, "Highly stretchable and sensitive strain sensor based on silver nanowire-elastomer nanocomposite," *ACS nano*, vol. 8, no. 5, pp. 5154–5163, 2014.
- [9] M. D. Ho, Y. Ling, L. W. Yap, Y. Wang, D. Dong, Y. Zhao, and W. Cheng, "Percolating network of ultrathin gold nanowires and silver nanowires toward invisible wearable sensors for detecting emotional expression and apexcardiogram," *Advanced Functional Materials*, 2017.
- [10] Y.-L. Park, B.-R. Chen, and R. J. Wood, "Design and fabrication of soft artificial skin using embedded microchannels and liquid conductors," *IEEE Sensors Journal*, vol. 12, no. 8, pp. 2711–2718, 2012.
- [11] Y.-L. Park, D. Tepayotl-Ramirez, R. J. Wood, and C. Majidi, "Influence of cross-sectional geometry on the sensitivity and hysteresis of liquid-phase electronic pressure sensors," *Applied Physics Letters*, vol. 101, no. 19, p. 191904, 2012.
- [12] J.-B. Chossat, Y.-L. Park, R. J. Wood, and V. Duchaine, "A soft strain sensor based on ionic and metal liquids," *IEEE Sensors Journal*, vol. 13, no. 9, pp. 3405–3414, 2013.
- [13] J.-B. Chossat, H.-S. Shin, Y.-L. Park, and V. Duchaine, "Soft tactile skin using an embedded ionic liquid and tomographic imaging," *Journal of Mechanisms and Robotics*, vol. 7, no. 2, p. 021008, 2015.
- [14] Y.-L. Park, C. Majidi, R. Kramer, P. Bérard, and R. J. Wood, "Hyperelastic pressure sensing with a liquid-embedded elastomer," *Journal of Micromechanics and Microengineering*, vol. 20, no. 12, p. 125029, 2010.
- [15] H.-S. Shin, J. Ryu, C. Majidi, and Y.-L. Park, "Enhanced performance of microfluidic soft pressure sensors with embedded solid microspheres," *Journal of Micromechanics and Microengineering*, vol. 26, no. 2, p. 025011, 2016.
- [16] T. Mikolov, M. Karafiát, L. Burget, J. Cernocký, and S. Khudanpur, "Recurrent neural network based language model," in *Interspeech*, vol. 2, 2010, p. 3.
- [17] I. Sutskever, O. Vinyals, and Q. V. Le, "Sequence to sequence learning with neural networks," in *Advances in neural information processing systems*, 2014, pp. 3104–3112.
- [18] Y. Bengio, P. Simard, and P. Frasconi, "Learning long-term dependencies with gradient descent is difficult," *IEEE transactions on neural networks*, vol. 5, no. 2, pp. 157–166, 1994.
- [19] S. Hochreiter and J. Schmidhuber, "Long short-term memory," *Neural computation*, vol. 9, no. 8, pp. 1735–1780, 1997.
- [20] A. Graves, "Generating sequences with recurrent neural networks," *arXiv preprint arXiv:1308.0850*, 2013.
- [21] N. Srivastava, G. E. Hinton, A. Krizhevsky, I. Sutskever, and R. Salakhutdinov, "Dropout: a simple way to prevent neural networks from overfitting," *Journal of machine learning research*, vol. 15, no. 1, pp. 1929–1958, 2014.
- [22] D. Kingma and J. Ba, "Adam: A method for stochastic optimization," *arXiv preprint arXiv:1412.6980*, 2014.
- [23] M. Abadi, A. Agarwal, P. Barham, E. Brevdo, Z. Chen, C. Citro, G. S. Corrado, A. Davis, J. Dean, M. Devin *et al.*, "Tensorflow: Large-scale machine learning on heterogeneous distributed systems," *arXiv preprint arXiv:1603.04467*, 2016.
- [24] S. M. M. De Rossi, N. Vitiello, T. Lenzi, R. Ronsse, B. Koopman, A. Persichetti, F. Vecchi, A. J. Ijspeert, H. Van der Kooij, and M. C. Carrozza, "Sensing pressure distribution on a lower-limb exoskeleton physical human-machine interface," *Sensors*, vol. 11, no. 1, pp. 207–227, 2010.
- [25] M. Y. Chuah and S. Kim, "Improved normal and shear tactile force sensor performance via least squares artificial neural network (lsann)," in *2016 IEEE International Conference on Robotics and Automation (ICRA)*, May 2016, pp. 116–122.